Anomalous Hall effect in magnetic insulator heterostructures: Contributions from the spin Hall and magnetic-proximity effects.

Shilei Ding[1], Zhongyu Liang[1], Chao Yun[1], Rui Wu[2,3] Mingzhu Xue[1], Zhongchong Lin[1], Andrew Ross[4], Sven Becker[2], Wenyun Yang[1], Xiaobai Ma[5], Dongfeng Chen[5], Kai Sun[5], Gerhard Jakob[2,6], Mathias Kläui[2,3,6], Jinbo Yang[1,7,8].*

[1]State Key Laboratory for Mesoscopic Physics, School of Physics, Peking University, Beijing 100871, P.R. China.

[2]Institute of Physics, Johannes Gutenberg-University Mainz, Staudingerweg 7, 55128 Mainz, Germany.

[3]Center for Quantum Spintronics, Department of Physics, Norwegian University of Science and Technology, NO-7491 Trondheim, Norway.

[4]Unité Mixte de Physique, CNRS, Thales, Université Paris-Saclay, Palaiseau, 91767, France.

[5]Department of Nuclear Physics, China Institute of Atomic Energy, Beijing, 102413, PR China

[6]Graduate School of Excellence Materials Science in Mainz, Staudinger Weg 9, 55128 Mainz, Germany.

[7]Collaborative Innovation Center of Quantum Matter, Beijing, 100871, P.R. China.

[8]Beijing Key Laboratory for Magnetoelectric Materials and Devices, Beijing 100871, P. R. China.

*Correspondence to [jbyang@pku.edu.cn]

In this letter, we study the origin of the anomalous Hall effect (AHE) in ferrimagnetic insulator $Tm_3Fe_5O_{12}$ (TmIG)/Pt heterostructures. A monotonic decrease of the anomalous Hall resistivity ($\Delta\rho_{AHE}$) with decreasing temperature is observed for TmIG/Pt, and a sign reversal of $\Delta\rho_{AHE}$ occurs at around 80 K. With the addition of a Cu interlayer, the $\Delta\rho_{AHE}$ similarly decreases as a function of temperature, but maintains the same sign across the full temperature range. This indicates that both the magnetic-proximity effect (MPE) and spin Hall effect (SHE) in the TmIG/Pt bilayer contribute to the AHE signal with opposing signs. The spin-Hall contribution to the AHE is dominant at room temperature but decreases with decreasing temperature. Meanwhile, the magnetic-proximity contribution to the AHE becomes dominant with decreasing temperatures, leading to a change of sign for $\Delta\rho_{AHE}$. We exclude a dominant influence of a ferrimagnetic compensation point in the temperature region by complementary magnetic hysteresis and neutron diffraction measurements. Our work, based on a simple method, sheds light on the origin of the AHE in magnetic insulator heterostructures, where the competition between the magnetic-proximity effect and spin Hall effect governs the sign and amplitude of the AHE.

$Tm_3Fe_5O_{12}$(TmIG)/Pt bilayer structures have recently attracted great interest in the field of spintronics, displaying exciting physical phenomena, including spin Hall magnetoresistance [1], spin-orbit torque magnetization switching [1-4], current-induced chiral domain wall motion [3,5] and interfacial Dzyaloshinskii-Moriya interaction (DMI) and topological Hall effects [3, 5-8]. The physical interpretation of these phenomena

can be based on a combination of the spin Hall effect (SHE) and interfacial mechanisms, where the latter ones are commonly related to the magnetic-proximity effect (MPE), a phenomenon that induces a ferromagnetic moment in a normal metal in contact with magnetic materials [9]. Pt is close to the Stoner criterion and has been shown to exhibit ferromagnetic ordering due to the MPE, where the strength of the MPE is closely related to the crystal structure at the interface [10,11]. Several groups have focused on different methods to quantify the magnitude of the magnetic-proximity effect , including X-ray Magnetic Circular Dichroism and X-ray Resonant Magnetic Reflectivity [12-15]. However, it is still under discussion in which systems the magnetic-proximity effect is present [16-18], what is the magnitude of magnetic moments induced by the MPE [19], and whether the MPE contributes to the anomalous Hall effect (AHE) signal in magnetic insulator/Pt heterostructures. If the MPE leads to magnetic ordering of Pt in contact with the magnetic insulator, the anomalous Hall resistivity, $\Delta\rho_{AHE}$, of the Pt can contribute to, or even give rise to, the AHE in such systems. This part of the AHE is considered to be a magnetic-proximity AHE signal [20,21]. In addition, the imaginary part of the spin mixing conductance can also lead to an AHE signal in magnetic insulator/Pt heterostructures, related to the SHE and spin transport at the interface and thus referred to as the spin-Hall AHE signal [22]. Several studies have attempted to separate the contributions from the spin Hall effect and magnetic-proximity effect to $\Delta\rho_{AHE}$ through first-principle calculations and angular dependent measurements [20,21,23-25] or the insertion of a Cu layer to decouple the magnetic insulator and Pt, limiting the MPE [26]. However, in magnetic insulator/Pt heterostructures, the relationship between the magnetic-proximity AHE and spin-Hall AHE is missing, and in particular, it is unclear whether the two contributions have different temperature dependencies.

In this letter, we use ferrimagnetic TmIG with perpendicular magnetic anisotropy to study the AHE signal in magnetic insulator heterostructures. From the temperature dependence of the AHE, we observed a sign change of $\Delta\rho_{AHE}$ in TmIG/Pt, which is absent when a Cu interlayer is inserted to reduce the MPE. Magnetic measurements and neutron diffraction studies exclude the effects of ferrimagnetic compensation, thus the sign change of $\Delta\rho_{AHE}$ can not be explained by the ferrimagnetic nature of TmIG. The experimental results indicate that both the spin Hall effect and magnetic-proximity effect contribute to the AHE in TmIG/Pt with opposing signs.

High-quality crystalline epitaxial TmIG films with perpendicular magnetic anisotropy were deposited on (111)-oriented gadolinium gallium garnet ($Gd_3Ga_5O_{12}$, GGG) substrates by pulsed laser deposition. The deposition conditions have been reported previously [4]. The Pt and Cu layers have been deposited *ex-situ* subsequently by sputtering in a chamber with a base pressure of 3×10^{-9} mbar, with an Ar pressure of 0.013 mbar. The thin film samples were patterned and etched into 6 μm × 20 μm Hall bars by standard photolithography and ion milling. The electrical measurements of TmIG(20)/Pt(5) and TmIG(20)/Cu(2)/Pt(5) (units in nanometers)

heterostructures were performed in a vector cryostat and a physical property measurement system (PPMS), and the current shunting effect was considered to accurately calculate $\Delta\rho_{AHE}$ for TmIG/Cu/Pt. The anomalous Hall resistivity $\Delta\rho_{AHE}$ can be obtained via $\Delta\rho_{AHE} = \Delta R_{AHE} t_{nm}$, where ΔR_{AHE} is the change of the anomalous Hall resistance and t_{nm} is the thickness of the normal metal. Magnetic hysteresis loops were measured via a PPMS equipped with a vibration sample magnetometer setup (VSM). The neutron diffraction study was performed using the Peking University High-Intensity Powder Neutron Diffractometer [27] at the China Advanced Research Reactor. Details of the sample preparation and data refinement can be found in the supplementary [28].

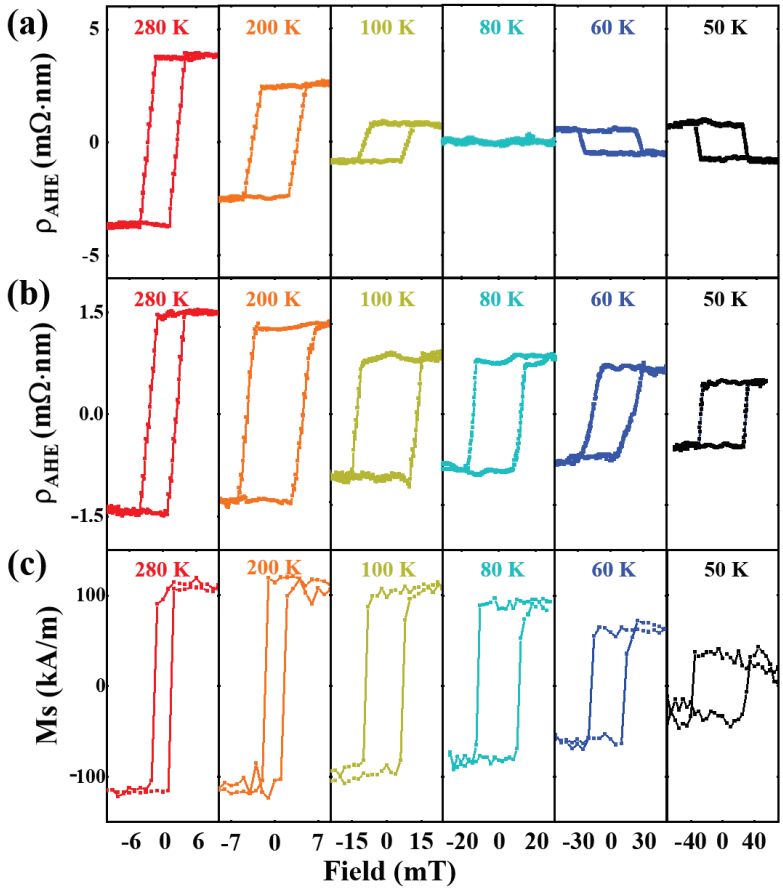

FIG. 1 (a) and (b) show the temperature dependence of the anomalous Hall hysteresis loops for TmIG(20)/Pt(5) and TmIG(20)/Cu(2)/Pt(5). (c) shows the magnetic hysteresis loops of 20 nm TmIG measured via VSM. The magnitude of $\Delta\rho_{AHE}$ is smaller in TmIG/Cu/Pt compared to the value of TmIG/Pt, due to additional interfacial scattering of the spin current and the strong spin memory loss at the Cu/Pt interface. The anomalous Hall resistance $\Delta\rho_{AHE}$ changes sign at around 80 K for TmIG/Pt, while the $\Delta\rho_{AHE}$ keeps the same sign for TmIG/Cu/Pt.

Figure 1 (a) and (b) show anomalous Hall hysteresis loops of TmIG(20)/Pt(5) and TmIG(20)/Cu(2)/Pt(5) heterostructures at different temperatures. The Hall voltages were collected via sweeping the out-of-plane field, which show well-defined square loops, and the coercivity values of TmIG/Pt and TmIG/Cu/Pt are similar for all temperatures. At 280 K, the coercivity from the AHE is determined to be 1.5 mT, while the magnetic measurement indicates the coercivity of 20-nm thick TmIG to be around 0.6 mT as shown in Fig. 1(c). We attribute the change of the coercive field after patterning the continuous film to the geometrical confinement effect, which can vary with temperature [1]. For the data collection, we reverse the polarity of the current to exclude any polarity-dependent effects. The resistivity change $2\Delta\rho_{AHE}$ between the two magnetic states for TmIG/Pt and TmIG/Cu/Pt at 280 K are $7.5 \pm 0.3\ \mathrm{m\Omega \cdot nm}$ and $2.8 \pm 0.2\ \mathrm{m\Omega \cdot nm}$ respectively. Cu is an efficient spin conductor, however, inserting a Cu layer creates the additional Cu/Pt interface, where the strong spin memory loss can occur [34,35], resulting in a decrease in the absolute magnitude of $\Delta\rho_{AHE}$ in TmIG/Cu/Pt. Tang et al. demonstrated a similar result and claimed that the decrease of $\Delta\rho_{AHE}$ for TmIG/Cu/Pt is evidence that the MPE has a significant contribution to the AHE in TmIG/Pt [26]. Indeed, Cu exhibits a quite long spin diffusion length, and Cu is so far from the Stoner criteria, it is unlikely to exhibit the MPE [36,37]. However, we will show below the decrease of $\Delta\rho_{AHE}$ when a Cu insertion layer is added is primarily caused by the spin scattering at the newly introduced Cu/Pt interface. Meanwhile, without considering the spin scattering, the absence of the magnetic-proximity AHE could fundamentally lead to larger $\Delta\rho_{AHE}$ for TmIG/Pt.

Remarkably, a different temperature dependence of $\Delta\rho_{AHE}$ is observed in TmIG/Pt and TmIG/Cu/Pt. For TmIG/Pt, $\Delta\rho_{AHE}$ decreases with decreasing temperature, and we observe a sign change at around 80 K in Fig. 1(a). A similar sign reversal has also been found in YIG/Pt system [10,20,21]. However, we find that the TmIG/Cu/Pt sample does not exhibit a sign reversal, as shown in Fig. 1(b). In the well-studied YIG/Pt system, different groups have published different conclusions with respect to MPE [18,19] and in one work the magnetic moment of Pt induced by the MPE has been determined to be $0.1\ \mu_B$ [19], and the MPE is also regarded as an important physical mechanism that can contribute to the AHE signal [21]. Regardless of a possible magnetic-proximity AHE signal in magnetic insulator heterostructures, Chen *et al*. theoretically studied the spin-Hall AHE in magnetic insulatros, where the spin-Hall AHE is related to the imaginary part of the spin mixing conductance. By noting that the real spin mixing conductance is orders of magnitudes larger than the imaginary spin mixing conductance, we can adopt the formulation of Chen *et al.* for the spin-Hall AHE [22]:

$$\frac{\Delta\rho_{SH-AHE}}{\rho_0} = \frac{2\theta_{SH}^2\lambda^2}{d_N}\frac{\sigma G_i tanh^2\frac{d_N}{2\lambda}}{\left(\sigma+2\lambda G_r coth^2\frac{d_N}{2\lambda}\right)^2}, \quad (1)$$

where the $\Delta\rho_{SH-AHE}$ is the resistivity of spin-Hall AHE, $\sigma = \rho_0^{-1}$, d_N, and λ are the conductivity, thickness, and spin diffusion length of Pt, G_r and G_i demonstrate the real and imaginary part of the spin mixing conductance. The spin mixing conductance is an indicator of the spin transmission and scattering at the interface.

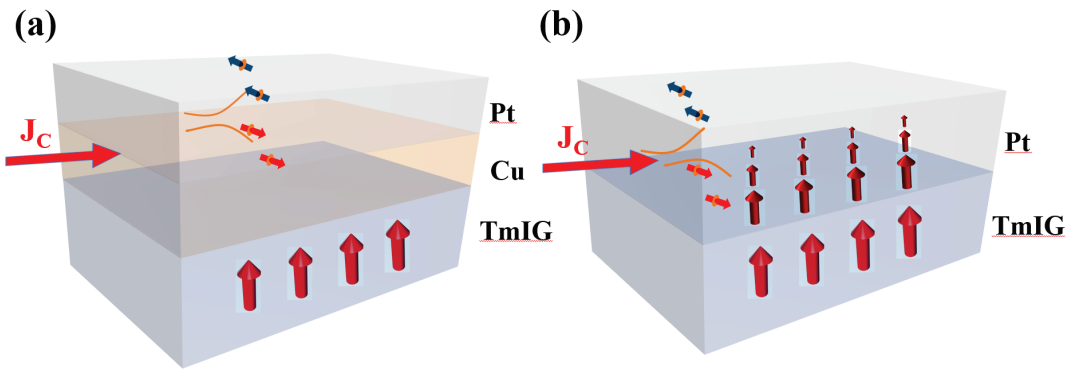

FIG. 2 Schematics for the different mechanisms of the origin of the AHE signals in TmIG/Cu/Pt and TmIG/Pt. (a) Cu is an efficient spin conductor with no magnetic-proximity effect, the spin current induced by the spin Hall effect in the Pt traverses the additional Cu layer and interacts with the magnetic moment of TmIG. The spin Hall effect induced AHE signal is related to the imaginary part of the spin mixing conductance. (b) Several atomic layers of Pt can exhibit ferromagnetic ordering due to the magnetic-proximity effect, which can also contribute to the AHE signal.

The schematics for the origin of the AHE signal in TmIG/Cu/Pt and TmIG/Pt are given in Fig. 2. For the TmIG/Cu/Pt sample, the spin current generated in the Pt is the only source of the AHE, and therefore represents a pure spin-Hall induced AHE signal. The $\Delta\rho_{AHE}$ decreases for lower temperatures, indicating a reduced imaginary part of spin mixing conductance at lower temperatures. This effect is related to the interfacial spin transport and the interaction between the spin current and the local magnetic moment in TmIG, thus we expect the temperature dependence of the AHE in TmIG/Cu/Pt to exhibit a similar trend as the temperature dependence of the magnetic hysteresis loop as shown in Fig. 1(b) and (c). As long as the value of the spin mixing conductance maintains the same sign, it is expected that the sign of $\Delta\rho_{AHE}$ does not change for TmIG/Cu/Pt. However, this is not the case in TmIG/Pt. If the MPE leads to a magnetic ordering of the Pt, both the spin-Hall AHE and magnetic-proximity AHE contribute to the $\Delta\rho_{AHE}$ in TmIG/Pt, and the phenomenon for the sign reversal of $\Delta\rho_{AHE}$ can only be explained assuming that the contribution to the magnitude of AHE is opposite for each mechanism. At 280 K, the spin-Hall AHE signal is dominating, which however decreases when the temperature drops. Meanwhile, the magnetic-proximity AHE is slowly increasing due to the strengthening of the exchange coupling between the Fe^{3+} *3d* orbitals and the Pt *5d* orbitals at lower temperatures [23]. The contributions from these two mechanisms are roughly equal at around 80 K, thus canceling each other to yield a zero AHE in TmIG/Pt (see Fig. 1(a)). Meanwhile, we clearly observe a magnetic hysteresis loop of TmIG at 80 K, which means the absence of an AHE in TmIG/Pt is not related to the possible vanishing of the magnetic moments in the ferrimagnetic TmIG. It is also known from the literature that there is no compensation point at 80 K in TmIG [38,39]. Further

decreasing the temperature leads to a dominant magnetic-proximity AHE signal and thus to the sign reversal of $\Delta\rho_{AHE}$ in TmIG/Pt.

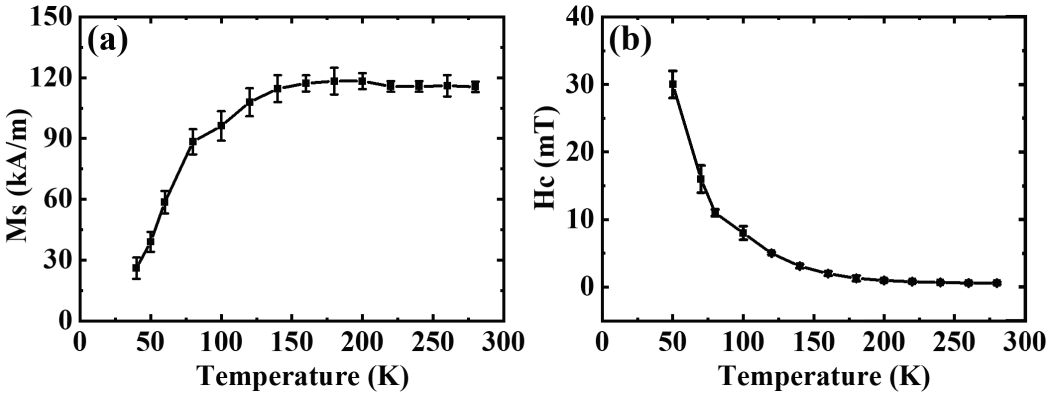

FIG. 3 (a) Temperature dependence of M_s for TmIG. (b) The coercivity of 20 nm TmIG was obtained by magnetic measurement via PPMS with a VSM setup. There is no compensation point within the studied temperature range.

The sign change of $\Delta\rho_{AHE}$ is commonly found for ferrimagnetic metal heterostructures where it is resulting from the change of the dominating sub-lattices with temperature leading to a change of the AHE signal when the temperature crosses the magnetic compensation point [40,41]. TmIG is a typical ferrimagnetic insulator in which the sum of the magnetic moments of Tm^{3+} ions and Fe^{3+} ions are colinear but pointing in opposite directions. To clarify whether the sign change of $\Delta\rho_{AHE}$ for TmIG/Pt at around 80 K is related to the magnetic compensation phenomenon, we performed magnetic hysteresis loops measurements at different temperatures to obtain the temperature dependence of saturation magnetization (M_s) for 20 nm TmIG, as shown in Fig. 3(a). The M_s initially maintains a nearly a constant value and then decreases with a decrease of temperature while the coercivity of TmIG increases (shown in Fig. 3(b)), which is a typical phenomenon for a ferrimagnet when the temperature approaches the compensation point. The magnetic moment at 150 K is roughly 2 times larger compared with the value at 60 K.

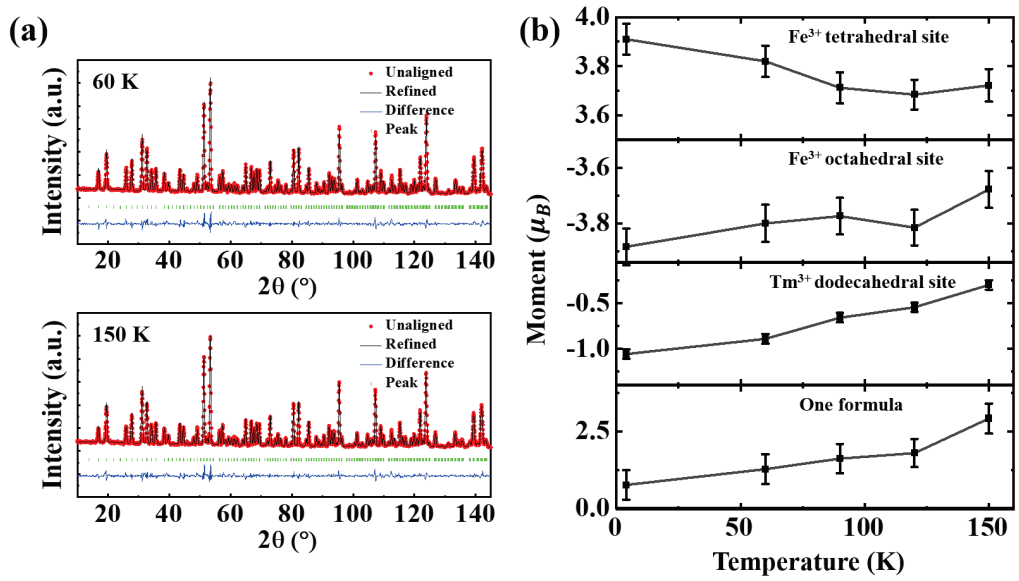

FIG. 4 (a) The refinement result of neutron diffraction patterns for TmIG collected at 60 K and 150 K. (b) The temperature dependency of the magnetic moment parameter of the Fe^{3+} ions, Tm^{3+} ions, and one formula unit of TmIG.

To clarify if there is any compensation of the moments, we perform neutron diffraction measurements that allow us to further understand the temperature dependence of the magnetic structures of powder TmIG. We note that 20 nm TmIG films are quite thick exhibiting a similar magnetic moment value compared to the bulk material [4] and the evolution of the magnetization as a function of temperature in 20 nm TmIG is similar to that of bulk materials [2], thus the magnetic properties of powder TmIG and 20 nm TmIG should be similar. Fig. 4(a) shows the Rietveld refinement of the data collected at 60 K and 150 K. As the structure of YIG is reported to distort from cubic to trigonal [42], the refinement of the neutron diffraction patterns for TmIG powder were performed with the trigonal space group ($R\bar{3}$, No.148). For refining the magnetic structure, the chosen magnetic space group $R\bar{3}$ (No. 148.17) was obtained using the program MAXMAGN by giving the space group $R\bar{3}$ and a propagation vector (0 0 0) [43]. The details for the refinement can be found in the supplemental materials [28]. The magnetic phase symmetry was defined to align the Fe^{3+} ions at tetrahedral sites. The magnetic moments of the Fe^{3+} ions at octahedral sites as well as Tm^{3+} ions at dodecahedral sites are in the antiparallel direction. We note that, at 150 K, the obtained magnetic moments are $3.72 \pm 0.07\ \mu_B$ and $-3.68 \pm 0.07\ \mu_B$ at tetrahedral and octahedral sites for Fe^{3+}, and the magnetic moment of Tm^{3+} at dodecahedral sites is $-0.30 \pm 0.05\ \mu_B$. Compared with the results at 150 K, the magnetic moments of Fe^{3+} at 60 K are determined to be $3.83 \pm 0.06\ \mu_B$ and $-3.8 \pm 0.07\ \mu_B$ respectively, which represent a slight increase. However, the magnetic moment of Tm^{3+} ions at 60 K increases significantly, which yields $-0.88 \pm 0.05\ \mu_B$. Fig. 4(b) demonstrates the temperature dependence of the magnetic moment of Fe^{3+} and Tm^{3+} ions. As the temperature goes down, the absolute value of the magnetic

moment of Fe^{3+} and Tm^{3+} ions increase, however, at different rates. The magnetic moment of Fe^{3+} ions is not that sensitive to the temperature below 150 K, while the magnetic moment of Tm^{3+} ions dramatically increases when the temperature decreases and the rare-earth ions Tm^{3+} exhibits a low magnetic ordering temperature (see Fig. 4(b)). As a result, we can find that the moment for one formula unit of TmIG decreases as the temperature drops. It is worth noting, the moment for one formula at 150 K is $2.91 \pm 0.27\ \mu_B$, which is 2.3 times larger than the value at 60 K ($1.25 \pm 0.24\ \mu_B$), within the error range, the ratio of the total magnetic moment at 150 K and 60 K obtained by neutron diffraction analysis is consistent with the magnetic measurement results as shown in Fig. 3(b). This further indicates no compensation point within the temperature range studied. Thus, we conclude that the $\Delta\rho_{AHE}$ reversal for TmIG/Pt is not resulting from any ferrimagnetic order of the TmIG, while the competition between the spin-Hall AHE and magnetic-proximity AHE plays an important role.

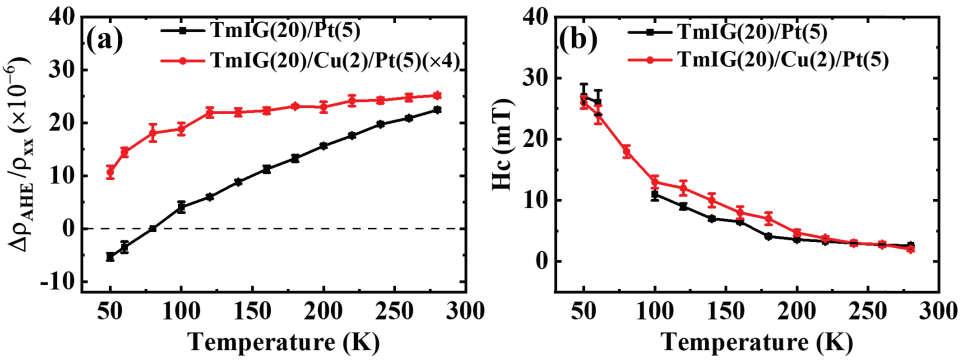

FIG. 5 (a) $\Delta\rho_{AHE}/\rho_{xx}$ for TmIG/Pt and TmIG/Cu/Pt at different temperatures. The ratio of $\Delta\rho_{AHE}/\rho_{xx}$ for TmIG/Cu/Pt is enlarged 4 times for ease of viewing. (b) demonstrates the coercivity of 20 nm TmIG obtained by the anomalous Hall measurement of TmIG/Pt and TmIG/Cu/Pt.

To further understand the competition of the MPE and SHE induced AHE signal, we studied the ratio of $\Delta\rho_{AHE}/\rho_{xx}$ for TmIG/Pt and TmIG/Cu/Pt as a function of temperature as indicated in Fig. 5. For TmIG/Cu/Pt, the value of $\Delta\rho_{AHE}/\rho_{xx}$ is enlarged 4 times for clarity. When the temperature is in the range of 150 K and 280 K, M_s has a relatively constant value. However, the $\Delta\rho_{AHE}/\rho_{xx}$ of TmIG/Cu/Pt slowly decreases for lower temperatures. When the temperature further drops below 150 K, the ratio $\Delta\rho_{AHE}/\rho_{xx}$ drops dramatically exhibiting similar behavior as the temperature dependence of M_s. Moreover, the decrease of $\Delta\rho_{AHE}/\rho_{xx}$ for the TmIG/Pt is faster compared with the value for TmIG/Cu/Pt when T < 150 K. As we discussed previously, the AHE signal in TmIG/Pt has two contributions, the spin-Hall AHE and magnetic-proximity AHE signals that exhibit opposite sign and thus opposite contributions to the total AHE signal. As the temperature goes down, the magnitude of spin-Hall AHE decreases while the magnetic-proximity AHE increases, which would lead to a

more abrupt change of $\Delta\rho_{AHE}/\rho_{xx}$ in TmIG/Pt compared with that in TmIG/Cu/Pt. Fig. 5(b) shows the coercivity of TmIG obtained via AHE in TmIG/Pt and TmIG/Cu/Pt. Note that inserting a Cu layer does not affect the value of the coercive field significantly showing that the magnetic properties of the TmIG are not significantly altered by the metallic layer on top. At T = 40 K, magnetic-proximity AHE plays a dominating role in the AHE for TmIG/Pt, while the spin-Hall AHE dominates the AHE in TmIG/Cu/Pt. Despite the distinct physical origin of the AHE at 40 K, the coercive fields for both of the samples are similar. It indicates the magnetic properties of the magnetized Pt are closely related to the underlying TmIG samples.

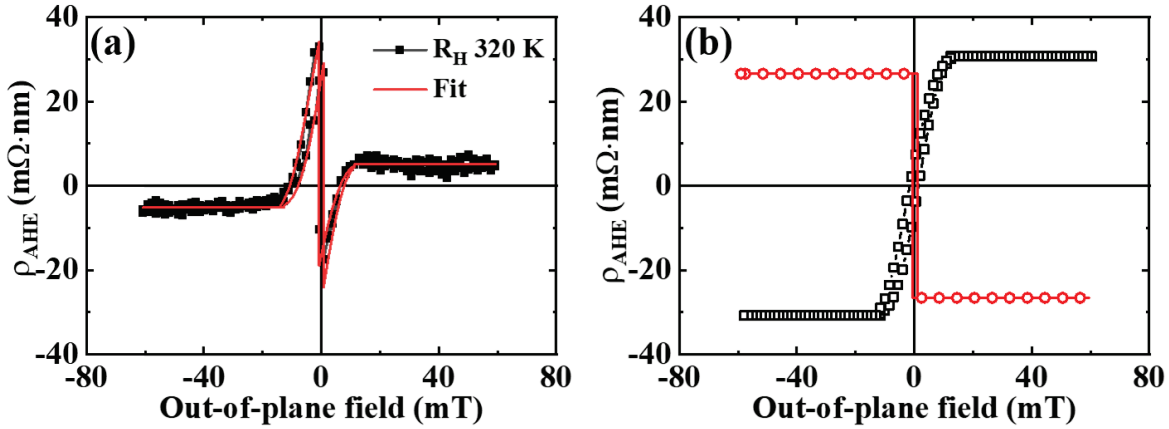

FIG. 6 Disentanglement of the topological Hall-like signal with the two-channel model. (a) The experimental data of anomalous Hall resistivity as a function of the field (the ordinary Hall resistance induced linear background is subtracted) and the fitting curve with the two-channel model. (b) The defined $\rho_{AHE}{}^{+}$(square, black) and $\rho_{AHE}{}^{-}$(circle, red) as the function of the field for the fitting.

Finally, we observed a topological Hall-like signal for TmIG(20)/Pt(5) measured at 320 K in a PPMS shown in Fig. 6 (a). Previous studies have indicated an interfacial DMI in TmIG/Pt [3,4], which could induce spin structures with a topological Hall effect [6,7]. Under the assumption of skyrmions in the system, the transverse Hall resistivity can be decomposed as: $\rho_{xy} = \rho_{OHE} + \rho_{AHE} + \rho_{THE}$, where ρ_{OHE} and ρ_{THE} represent the ordinary Hall resistivity and the topogolocal Hall resistivity. However, as demonstrated by several groups, the DMI in the TmIG/Pt system shows an interfacial origin, and 20 nm TmIG is likely to be too thick to exhibit sizable interfacial DMI [3-5,8]. Thus we conclude the Hall signal here is not resulting from chiral spin textures. Alternatively, the topological Hall-like resistivity can also be decomposed as: $\rho_{xy} = \rho_{OHE} + \rho_{AHE}{}^{+} + \rho_{AHE}{}^{-}$, where the last two terms denote the positive and negative contribution to the ρ_{xy}, and this two-channel model could successfully capture the Hall resistivity behavior as a function of field in certain systems [44-46]. As we

discussed previously, we could conclude that the spin-Hall AHE is positive ($\rho_{AHE}{}^{+}$) and the magnetic-proximity AHE is negative ($\rho_{AHE}{}^{-}$), in order to fit the curve as indicated in Fig. 6(a). The fitting result from the two-channel model agrees well with the experimental data without additional topological Hall-like inputs. The defined $\rho_{AHE}{}^{+}$ and $\rho_{AHE}{}^{-}$ as the function of the field can be found in Fig. 6(b). The spin-Hall AHE is directly related to the magnetic properties of TmIG film, as the spin mixing conductance is related to the thickness of the magnetic layer which is governed by the phase shift of the reflected electrons at the interface [4]. We would naturally expect that the spin-Hall AHE represents the bulk magnetic properties of the underlying TmIG film, confirmed by the similar shape to the magnetic hysteresis of the TmIG film. Indeed, we find the shape of the defined $\rho_{AHE}{}^{+}$ is similar to the magnetic hysteresis loop at 320 K, and we observe a spin reorientation in TmIG films at higher temperatures, where the perpendicular magnetic anisotropy slowly changes to a dominating in-plane magnetic anisotropy [28]. The magnetic-proximity AHE is, however, connected to the interfacial magnetism of TmIG. The interfacial magnetism of in-plane magnetized YIG could present an out-of-plane easy axis [47]. The interfacial magnetism of TmIG could similarly be different from the bulk magnetism under certain conditions. Thus the magnetic-proximity AHE could show different anisotropy compared with the spin-Hall AHE. The differing origins of the two effects, alongside their different signs, in turn leads to the topological Hall-like signal. Considering that the contribution at these elevated temperatures indicates a transition to in-plane anisotropy for the spin-Hall AHE (see also magnetization measurements in the supplementary), the magnetic-proximity AHE relies on a stronger perpendicular magnetic anisotropy at the interface than present in the bulk of the film (see Fig 6b). However, a full exploration of the interfacial versus bulk anisotropy of these films is outside of the scope of this work. Thinner films to increase the interface to volume ratio could be utilized to explore this further but then contributions of interfacial DMI will also be present, clouding the origin of this topological Hall-like shape. Moreover, this topological Hall-like signal can not be observed for TmIG/Cu/Pt at 320 K where the magnetic-proximity AHE is absent [28]. This result further demonstrates that both the spin Hall and the magnetic-proximity effect would contribute to the AHE curve, and their contributions are opposite.

In conclusion, we have systematically studied the temperature dependence of the anomalous Hall effect signal in TmIG/Pt and TmIG/Cu/Pt. Both the SHE and the MPE are found to contribute to the AHE in TmIG/Pt, while the AHE in TmIG/Cu/Pt heterostructures is dictated by only the SHE. The spin-Hall AHE decreases monotonically with decreasing temperature, and the magnetic-proximity AHE is strengthened as the exchange interaction between Fe^{3+} *3d* orbitals and the Pt *5d* orbitals is stronger at low temperatures. This further induces the sign reversal of $\Delta\rho_{AHE}$ at around 80 K. Our results suggest the key role of the MPE for the AHE in magnetic insulator heterostructures, which helps to understand the origin of AHE, and consequences for technological work and the design of spintronic devices based on magnetic insulators heterostructures.

Acknowledgments

We acknowledge the support from the National Key Research and Development Program of China (Grant No. 2017YFA0206303, 2017YFA0403701). National Natural Science Foundation of China (Grant No. 51731001, 11805006, 11975035), Graduate School of Excellence Materials Science in Mainz (MAINZ, GSC/266), Deutsche Forschungsgemeinschaft (DFG, German Research Foundation) Spin+X (A01, B02) TRR 173 – 268565370 and Project No. 358671374 and the Research Council of Norway through its Centres of Excellence funding scheme, Project No. 262633 "QuSpin.".

Reference

1. C. O. Avci, A. Quindeau, C. F. Pai, M. Mann, L. Caretta, A. S. Tang, M. C. Onbasli, C. A. Ross, and G. S. D. Beach, Nat. Mater. **16**, 309–314 (2017).
2. Q. Shao, C. Tang, G. Yu, A. Navabi, H. Wu, C. He, J. Li, P. Upadhyaya, P. Zhang, S. A. Razavi, Q. L. He, Y. Liu, P. Yang, S. K. Kim, C. Zheng, Y. Liu, L. Pan, R. K. Lake, X. Han, Y. Tserkovnyak, J. Shi, and K. L. Wang, Nat. Commun. **9**, 3612 (2018).
3. S. Ding, A. Ross, R. Lebrun, S. Becker, K. Lee, I. Boventer, S. Das, Y. Kurokawa, S. Gupta, J. Yang, G. Jakob, and M. Kläui, Phys. Rev. B **100**, 100406(R) (2019).
4. S. Ding, L. Baldrati, A. Ross, Z. Ren, R. Wu, S. Becker, J. Yang, G. Jakob, A. Brataas, and M. Kläui, Phys. Rev. B **102**, 054425 (2020).
5. C. O. Avci, E. Rosenberg, L. Caretta, F. Büttner, M. Mann, C. Marcus, D. Bono, C. A. Ross, and G. S. D. Beach, Nat. Nanotechnol. **14**, 561–566 (2019).
6. Q. Shao, Y. Liu, G. Yu, S. K. Kim, X. Che, C. Tang, Q. L. He, Y. Tserkovnyak, J. Shi, and K. L. Wang, Nat. Electron. **2**, 182–186 (2019).
7. A. J. Lee, A. S. Ahmed, J. Flores, S. Guo, B. Wang, N. Bagués, D. W. Mccomb, and F. Yang, Phys. Rev. Lett. **124**, 107201 (2020).
8. L. Caretta, E. Rosenberg, F. Büttner, T. Fakhrul, P. Gargiani, M. Valvidares, Z. Chen, P. Reddy, D. A. Muller, C. A. Ross, and G. S. D. Beach, Nat. Commun. **11**, 1090 (2020).
9. G. Bergmann, Phys. Rev. Lett. **41**, 264 (1978).
10. S. Y. Huang, X. Fan, D. Qu, Y. P. Chen, W. G. Wang, J. Wu, T. Y. Chen, J. Q. Xiao, and C. L. Chien, Phys. Rev. Lett. **109**, 107204 (2012).
11. M. Collet, R. Mattana, J.-B. Moussy, K. Ollefs, S. Collin, C. Deranlot, A. Anane, V. Cros, F. Petroff, F. Wilhelm, and A. Rogalev, Appl. Phys. Lett. **111**, 202401 (2017).
12. S. Geprägs, S. Meyer, S. Altmannshofer, M. Opel, F. Wilhelm, A. Rogalev, R. Gross, and S. T. B. Goennenwein, Appl. Phys. Lett. **101**, 262407 (2012).

13. T. Kuschel, C. Klewe, J. M. Schmalhorst, F. Bertram, O. Kuschel, T. Schemme, J. Wollschläger, S. Francoual, J. Strempfer, A. Gupta, M. Meinert, G. Götz, D.Meier, and G. Reiss, Phys. Rev. Lett. **115**, 097401 (2015).

14. D. Graulich, J. Krieft, A. Moskaltsova, J. Demir, T. Peters, T. Pohlmann, F. Bertram, J. Wollschläger, J. R. L. Mardegan, S. Francoual, and T. Kuschel, Appl. Phys. Lett. **118**, 12407 (2021).

15. Q. Shao, A. Grutter, Y. Liu, G. Yu, C.-Y. Yang, D. A. Gilbert, E. Arenholz, P. Shafer, X. Che, C. Tang, M. Aldosary, A. Navabi, Q. L. He, B. J. Kirby, J. Shi, and K. L. Wang, Phys. Rev. B **99**, 104401 (2019).

16. M. Valvidares, N. Dix, M. Isasa, K. Ollefs, F. Wilhelm, A. Rogalev, F. Sánchez, E. Pellegrin, A. Bedoya-Pinto, P. Gargiani, L. E. Hueso, F. Casanova, and J. Fontcuberta, Phys. Rev. B **93**, 214415 (2016).

17. A. I. Figueroa, F. Bonell, M. G. Cuxart, M. Valvidares, P. Gargiani, G. van der Laan, A. Mugarza, and S. O. Valenzuela, Phys. Rev. Lett. **125**, 226801 (2020).

18. S. Geprägs, C. Klewe, S. Meyer, D. Graulich, F. Schade, M. Schneider, S. Francoual, S. P. Collins, K. Ollefs, F. Wilhelm, A. Rogalev, Y. Joly, S. T. B. Goennenwein, M. Opel, T. Kuschel, and R. Gross, Bilayers, Phys. Rev. B **102**, 214438 (2020).

19. Y. M. Lu, Y. Choi, C. M. Ortega, X. M. Cheng, J. W. Cai, S. Y. Huang, L. Sun, and C. L. Chien, Phys. Rev. Lett. **110**, 147207 (2013).

20. B. F. Miao, S. Y. Huang, D. Qu, and C. L. Chien, Phys. Rev. Lett. **112**, 236601 (2014).

21. X. Liang, G. Shi, L. Deng, F. Huang, J. Qin, T. Tang, C. Wang, B. Peng, C. Song, and L. Bi, Phys. Rev. Appl. **10**, 24051 (2018).

22. Y.-T. Chen, S. Takahashi, H. Nakayama, M. Althammer, S. T. B. Goennenwein, E. Saitoh, and G. E. W. Bauer, Phys. Rev. B **87**, 144411 (2013).

23. X. Liang, Y. Zhu, B. Peng, L. Deng, J. Xie, H. Lu, M. Wu, and L. Bi, ACS Appl. Mater. Interfaces **8**, 8175 (2016).

24. S. Meyer, R. Schlitz, S. Geprägs, M. Opel, H. Huebl, R. Gross, and S. T. B. Goennenwein, Appl. Phys. Lett. **106**, 132402 (2015).

25. J. H. Han, G. Y. Shi, X. J. Zhou, Q. H. Yang, Y. H. Rao, G. Li, H. W. Zhang, F. Pan, and C. Song, Phys. Rev. B **94**, 134406 (2016).

26. C. Tang, P. Sellappan, Y. Liu, Y. Xu, J. E. Garay, and J. Shi, Phys. Rev. B **94**, 140403 (2016).

27. W. Yang, H. Zhao, Y. Lai, G. Qiao, Y. Xia, H. Du, J. Han, C. Wang, S. Liu, Y. Yang, Y. Hou, and J. Yang, IEEE Trans. Nucl. Sci. **65**, 1324 (2018).

28. See Supplemental Material at http://link.aps.org/supplemental/ PhysRevB.xx.xxxxxx for detail about the refinement of neutron diffraction data and the temperature dependence of hysteresis loops above 280 K for TmIG, which includes Refs.[29,30,31,32,33].

29. M. A. Musa, R. S. Azis, N. H. Osman, J. Hassan, and T. Zangina, Results Phys. **7**, 1135 (2017).

30. B. A. Tavger, Kristallografiya **3**, 339 (1958).

31. W. Prandl, in: H. Dachs (Ed.), Neutron Diffraction, Springer, Berlin, p113 (1978).

32. H. M. Rietveld, Acta Crystallogr. **22**, 151 (1967).

33. J. Rodríguez-Carvajal, Phys. B Condens. Matter **192**, 55 (1993).

34. H. Kurt, R. Loloee, K. Eid, W. P. Pratt, and J. Bass, Appl. Phys. Lett. **81**, 4787 (2002).

35. K. Dolui and B. K. Nikolić, Phys. Rev. B **96**, 220403 (2017).

36. M. Gradhand, D. V Fedorov, P. Zahn, and I. Mertig, Phys. Rev. B **81**, 245109 (2010).

37. Q. Sun, X. G. Gong, Q. Q. Zheng, D. Y. Sun, and G. H. Wang, Phys. Rev. B **54**, 10896 (1996).

38. P. Hansen and W. Tolksdorf, J. Appl. Phys. **69**, 4577 (1991).

39. A. Quindeau, C. O. Avci, W. Liu, C. Sun, M. Mann, A. S. Tang, M. C. Onbasli, D. Bono, P. M. Voyles, Y. Xu, J. Robinson, G. S. D. Beach, and C. A. Ross, Adv. Electron. Mater. **3**, 1600376 (2017).

40. Y. K. Liu, H. F. Wong, K. K. Lam, K. H. Chan, C. L. Mak, and C. W. Leung, J. Magn. Magn. Mater. **468**, 235 (2018).

41. J. Yu, L. Liu, J. Deng, C. Zhou, H. Liu, F. Poh, and J. Chen, J. Magn. Magn. Mater. **487**, 165316 (2019).

42. S. Shamoto, T. U. Ito, H. Onishi, H. Yamauchi, Y. Inamura, M. Matsuura, M. Akatsu, K. Kodama, A. Nakao, T. Moyoshi, K. Munakata, T. Ohhara, M. Nakamura, S. Ohira-Kawamura, Y. Nemoto, and K. Shibata, Phys. Rev. B **97**, 54429 (2018).

43. J. M. Perez-Mato, S. V Gallego, E. S. Tasci, L. Elcoro, G. de la Flor, and M. I. Aroyo, Symmetry-Based Computational Tools for Magnetic Crystallography, Annu. Rev. Mater. Res. **45**, 217 (2015).

44. L. Wu, F. Wen, Y. Fu, J. H. Wilson, X. Liu, Y. Zhang, D. M. Vasiukov, M. S. Kareev, J. H. Pixley, and J. Chakhalian, Phys. Rev. B 102, 220406 (2020).

45. K. M. Fijalkowski, M. Hartl, M. Winnerlein, P. Mandal, S. Schreyeck, K. Brunner, C. Gould, and L. W. Molenkamp, Phys. Rev. X **10**, 11012 (2020).

46. B. Jia, S. Zhang, Z. Ying, H. Xie, B. Chen, M. Naveed, F. Fei, M. Zhang, D. Pan, and F. Song, Appl. Phys. Lett. **118**, 83101 (2021).

47. K. Uchida, J. Ohe, T. Kikkawa, S. Daimon, D. Hou, Z. Qiu, and E. Saitoh, Phys. Rev. B **92**, 14415 (2015).